LUND UNIVERSITY

The design of a trimodal broadside antenna element for compact massive MIMO arrays
Utilizing the Theory of Characteristic Modes

Chiu, Chi Yuk; Shen, Shanpu; Lau, Buon Kiong; Murch, Ross

LUND UNIVERSITY

PO Box 117
221 00 Lund
+46 46-222 00 00

Design of a Tri-Modal Broadside Antenna Element for Compact Massive MIMO Arrays

Chi-Yuk Chiu, *Senior Member, IEEE,* Shanpu Shen, *Member, IEEE,* Buon Kiong Lau, *Senior Member, IEEE,* and Ross Murch, *Fellow, IEEE*

Abstract—**Massive multiple-input multiple-output (MIMO) arrays are becoming critical elements in cellular base station infrastructure. We utilize the theory of characteristic modes (TCM) to design a novel tri-modal broadside antenna element which is suitable for the construction of compact massive MIMO arrays. The proposed antenna element consists of three ports which is formed by reviewing an existing compact two-port Y-shaped patch antenna from a TCM perspective. Using this perspective the Y-shaped antenna is modified into a snowflake-shaped patch antenna and excited by three ports via capacitive coupling. The advantage of the design approach is that the size of the three-port antenna is approximately the same as a conventional dual-polarized patch antenna, hence allowing 50% more antenna elements for the same array aperture. By cutting the ground plane into a hexagonal shape, multiple of the proposed three-port canonical antennas are concatenated together to form 21- and 102-port massive MIMO arrays with all radiation patterns pointing in the broadside direction. Key performance characteristics of the massive MIMO arrays, such as the Hermitian product of the simulated massive MIMO channel and mutual coupling, validate the effectiveness of the compact design.**

Index Terms—**Characteristic modes, massive multiple-input multiple-output (MIMO), multimode antenna, multiport antenna, MIMO antenna.**

I. INTRODUCTION

ONE promising radio access technology for future wireless communication systems (including upcoming 5G) is massive multiple-input multiple-output (MIMO) antenna systems, which can significantly increase spectral efficiency [1]-[3]. Massive MIMO uses a large number of antennas at the base station to achieve multi-user MIMO [4] operation with computationally efficient linear precoders and decoders [2].

A. Massive MIMO Array Requirements

Massive MIMO's requirement for many antenna elements (typically 100 or more [1]) makes the array size very large. Therefore, it is desirable to reduce the size of the massive MIMO array, particularly for conventional mobile frequency bands (i.e., under 6 GHz). One solution for size reduction has been to utilize multimode antennas [5]-[8] as the unit cell, to allow more antenna ports to be implemented in a given area. However, the radiation pattern of individual antenna ports in a massive MIMO array should ideally be omni-directional or cover the desired base station sector, such that every antenna port can receive as many multipath signals as possible. For outdoor base station antennas, this usually implies the need for a broadside radiation pattern that is wide enough to cover the sector of interest. Unfortunately, the resulting overlap in the radiation patterns in the broadside direction will usually increase mutual coupling [9].

B. Conventional Dual-Polarized Array Elements

Two orthogonal polarizations may be used to provide orthogonal broadside patterns, such as those offered by dual-polarized patch antennas. Various designs of two-port antennas with orthogonal broadside radiation patterns have been proposed in the past decade [10]-[18]. In [10], a compact Y-shaped two-port multimode diversity antenna has been demonstrated to generate two low correlated broadside patterns by placing one feed at the voltage null resulting from exciting the other feed. To further reduce the size of massive MIMO arrays, one approach is to attempt to add additional ports to the basic radiation element. However, if one more port with broadside radiation is to be added, the degrees of freedom from polarization alone is insufficient to facilitate low mutual coupling among the three ports. Therefore, to our knowledge, compact MIMO antenna designs exhibiting more than two similar broadside patterns simultaneously and having low mutual coupling and correlation have not been investigated.

C. Theory of Characteristic Modes and Massive MIMO Array Element Design

A tool that has been found useful for the design and analysis of MIMO antennas [19], [20] is the theory of characteristic modes (TCM). TCM was first introduced in the 1960's [21] to describe the interaction of an object with an incident wave. In TCM, the current distribution over the object is decomposed into an infinite number of orthogonal modal currents, each

of which radiates an orthogonal characteristic modal far-field pattern. In [22], Garbacz further elaborated the idea by pointing out that, at a given frequency, every perfectly conducting object has associated with it a particular set of surface currents and corresponding radiated fields, which are characteristic of the object shape and independent of any specific excitation. Correspondingly if one of the orthogonal modal far-field patterns is used to excite the object, the scattered radiation will have exactly the same orthogonal far-field pattern and its magnitude will be related to the eigenvalue of that characteristic mode. Therefore, TCM is able to provide insights into the natural resonant phenomena of any conducting object. In [23], [24], the modal solution for the current on a conducting body was obtained by using the eigencurrents as both expansion and testing functions in the method of moments (MoM). A set of surface currents flowing on the object can be calculated without determining the antenna excitation structure and location. The associated orthogonal radiated farfield patterns can also be obtained, which is important for the design of multimode antennas.

In [20], [25], the idea of geometrical modification has been used to reduce the resonant frequency of a second mode in order to facilitate the design of two-element MIMO terminal antennas for frequency bands below 1 GHz. However, preserving the same radiation pattern across multiple ports, let alone broadside patterns, has not been a criterion in these previous works, which focused on terminal antenna applications. The two-port terminal antenna proposed in [26] utilizes two predefined coupling elements to achieve orthogonal radiation patterns at 2.28 GHz. TCM was used to show that, despite the two designed ports simultaneously exciting the same two dominant modes, pattern orthogonality is preserved thanks to the phase difference in the excitation of one of the two modes by the two ports.

In [8], TCM was employed to design a compact multimode multiport antenna as the unit cell for an indoor ultra-wide bandwidth (UWB) massive MIMO array. Different characteristic modes on each unit cell were excited simultaneously by feeding slots on a patch with desired phases. A feed network containing Wilkinson power dividers and branch line couplers was utilized to provide each port with its set of desired phases, leading to four orthogonal far-field patterns. In the four-port unit cell design, two broadside and two non-broadside radiation patterns were achieved, which are suitable for multipath-rich indoor scenarios.

D. Proposed Design and Contributions

Different to previous antennas designed using TCM, this work targets a three-port array element (unit cell) design for outdoor massive MIMO application. The key contribution is that the three ports, realized in a compact hexagonal element with the help of TCM, can exhibit broadside radiation simultaneously while maintaining low mutual coupling. To achieve this design using TCM, the starting point was to study the operating mechanism of an existing two-port Y-shaped patch antenna using the new perspective of TCM. Then, the two-port Y-shaped antenna design was extended with insights

provided by TCM to achieve the proposed compact three-port antenna element. Apart from providing insight on how to exploit another mode (i.e., a third mode) for the element design, TCM also guided the design of the feeds (type and location) for the proposed three-port antenna.

Furthermore, having the desirable properties of compact size, low mutual coupling and broadside radiation pattern simultaneously, seven of the proposed three-port antennas (forming a 21-port antennas) were simulated and prototyped. A further array structure with 34 of the proposed three-port element were simulated (forming a 102-port array) to demonstrate the scalability and prospect of the proposed three-port element for massive MIMO arrays.

This article is organized as follows. In Section II, TCM is briefly reviewed. Then, an existing compact two-port Y-shaped antenna [10] is analyzed in Section III and evolved into a compact three-port snowflake-shaped antenna in Section IV. In Section V, multiple three-port canonical antennas are concatenated together to form 21- and 102-port massive MIMO arrays with all radiation patterns pointing in the broadside direction. In addtition, several key massive MIMO characteristics of the 102-port array are evaluated in simulation using a standard MIMO channel model. Finally, a summary is given in Section VI.

II. THEORY OF CHARACTERISTIC MODES

When the surface of a conducting body S is impressed by an electric field, a surface current $\mathbf{J}$ is obtained. In TCM, an impedance operator $Z(\mathbf{J})$ is introduced as [23]

$$Z(\mathbf{J}) = [L(\mathbf{J})]_{\mathrm{tan}} = R(\mathbf{J}) + jX(\mathbf{J}), \qquad (1)$$

where $[\ ]_{\mathrm{tan}}$ denotes the tangential components on S, and L is a linear operator [23].

Because the $L(\mathbf{J})$ operator has the unit of impedance, and R and X are the real and imaginary parts of Z, they are its resistance and reactance, respectively. To obtain orthogonal modal far-field patterns [23], the weighted eigenvalue equation

$$X(\mathbf{J}_n) = \lambda_n R(\mathbf{J}_n) \qquad (2)$$

is considered, where $\mathbf{J}_n$ denotes the nth eigenfunction, also called the nth characteristic current in TCM, associated with the nth eigenvalue λ_n. The smaller the magnitude of λ_n, the smaller the difference in stored magnetic and electric energies and the more resonant is the nth mode. In addition, if $\lambda_n > 0$, the mode is inductive and if $\lambda_n < 0$, the mode is capacitive. Three key aspects of TCM are summarized in the following subsections [23].

A. Current Orthogonality

The characteristic currents $\mathbf{J}_n$ are orthogonal to each other with respect to the weighting by the R operator so that

$$\langle \mathbf{J}_m, R(\mathbf{J}_n) \rangle = \delta_{mn}, \qquad (3)$$

$$\langle \mathbf{J}_m, X(\mathbf{J}_n) \rangle = \lambda_n \delta_{mn}, \qquad (4)$$

$$\langle \mathbf{J}_m, Z(\mathbf{J}_n) \rangle = (1 + j\lambda_n) \delta_{mn}, \qquad (5)$$

where $\langle \mathbf{A}, \mathbf{B} \rangle = \iint_S \mathbf{A} \cdot \mathbf{B}^* \mathrm{d}s$ defines the symmetric product of two vector functions $\mathbf{A}$ and $\mathbf{B}$ on S, the asterisk denotes

the complex conjugate, δ_{mn} is the Kronecker delta function (0 if $m \neq n$, and 1 if $m = n$), and each characteristic current is normalized according to $\langle \mathbf{J}_n, R(\mathbf{J}_n) \rangle = 1$.

B. Far-field Orthogonality

The electric field $\mathbf{E}_n$ and the magnetic field $\mathbf{H}_n$ produced by $\mathbf{J}_n$ are called the nth characteristic fields. For far-field, the characteristic fields are orthogonal to each other so that

$$\frac{1}{Z_\eta} \oiint_{S_\infty} \mathbf{E}_m \cdot \mathbf{E}_n^* \, ds = \delta_{mn}, \tag{6}$$

$$Z_\eta \oiint_{S_\infty} \mathbf{H}_m \cdot \mathbf{H}_n^* \, ds = \delta_{mn}, \tag{7}$$

where Z_η denotes the wave impedance of free space and S_∞ is the surface of the sphere with an infinite radius.

C. Modal Solutions

The surface current $\mathbf{J}$ and the corresponding excited fields $\mathbf{E}$ and $\mathbf{H}$ can be expanded as

$$\mathbf{J} = \sum_n \frac{\langle \mathbf{J}_n, \mathbf{E}_{\text{imp}} \rangle}{1 + j\lambda_n} \mathbf{J}_n, \tag{8}$$

$$\mathbf{E} = \sum_n \frac{\langle \mathbf{J}_n, \mathbf{E}_{\text{imp}} \rangle}{1 + j\lambda_n} \mathbf{E}_n, \tag{9}$$

$$\mathbf{H} = \sum_n \frac{\langle \mathbf{J}_n, \mathbf{E}_{\text{imp}} \rangle}{1 + j\lambda_n} \mathbf{H}_n, \tag{10}$$

where $\mathbf{E}_{\text{imp}}$ is the impressed electric field from an excitation source.

III. TCM ANALYSIS OF A COMPACT TWO-PORT Y-SHAPED PATCH ANTENNA

In [10], a compact two-port Y-shaped patch antenna was introduced. The results show that the two-port antenna exhibits broadside radiation, low correlation and over 20 dB isolation. The design was based on placing one feed at a location with voltage null when the other feed was excited, while achieving good impedance matching. In this article, the design of the compact two-port Y-shaped patch antenna is revisited from the TCM point of view. The new insights from characteristic mode (CM) analysis forms a cornerstone for the proposed compact three-port antenna with broadside patterns, which will be discussed in the next section.

A. Antenna Structure

Figures. 1(a)-(b) illustrates the geometry of the capacitive loaded Y-shaped patch antenna with two direct feeds based on the design in [10]. The basic idea is to merge two rectangular patch antennas by overlapping part of the surface areas such that a size reduction can be achieved. The radiating patch is situated on a circular ground plane with the diameter of 140 mm and both are made of 1 mm thick copper sheets. The probe lengths are 7 mm and the three branches of the Y-shaped patch are folded downward towards the ground plane to provide capacitive loads to the antenna. These loads facilitate further

antenna miniaturization. The air gap between the bottom of each branch and the ground plane is 1 mm. The antenna resonates at 2.38 GHz, with coupling coefficient being lower than -15 dB when considering the 10 dB impedance bandwidth [10]. The results were also re-verified using the time-domain solver CST Microwave Studio [27]. Due to mirror symmetry, the two antenna ports exhibit identical radiation performance but reflected along the $y - z$ plane. A comparative design example resonating at the same frequency is a larger conventional dual-polarized square patch antenna with the side length of 56 mm, a 7 mm-thick air substrate and its two feeds aligned along the two center-lines of the square surface. Such a reference square patch design offers two orthogonally polarized patterns with low mutual coupling and correlation.
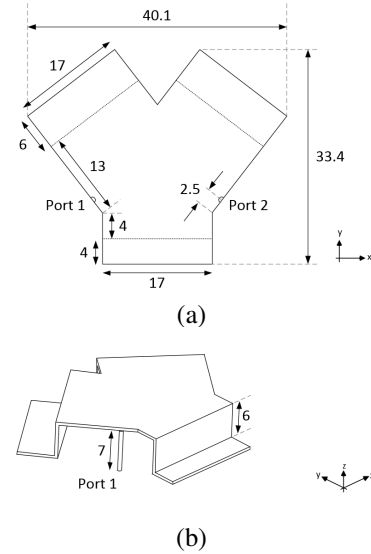

Fig. 1. Two-port folded Y-shaped patch antenna [10] (a) Geometry in plan view (units: mm) and (b) geometry in perspective view.

B. Characteristic Mode Analysis and Antenna Performance

The electromagnetic simulation software FEKO [28] was used to perform CM analysis of the Y-shaped patch antenna. An infinite ground plane was used to eliminate the radiation modes contributed by the finite-size ground plane. The eigenvalues of the characteristic modes are shown in Fig. 2(a) and the corresponding electric far-field patterns of Modes 1 to 3 at 2.35 GHz are shown in Figs. 2(b)-(d). As can be seen in Fig. 2(a), Modes 1 and 2 are the dominant CMs at around 2.35 GHz. Since the feed points (Ports 1 and 2) are located in regions of high electric near-fields of both Modes 1 and 2, which allow both ports to simultaneously excite these two modes. However, these two ports do not strongly couple to (or correlate with) each other despite each of them exciting the same modes by the same amount. The reason is that the Ports 1 and 2 excite Mode 2 with 180° phase difference, canceling the correlation due to Mode 1, as calculated by

$$\rho_{\text{tc,MIMO}} = \frac{\sum_n \alpha_{n,i}^* \alpha_{n,j}}{\sqrt{\sum_n |\alpha_{n,i}|^2} \sqrt{\sum_n |\alpha_{n,j}|^2}}, \tag{11}$$

where $\rho_{\text{tc,MIMO}}$ and $\alpha_{n,i}$ denote as the complex correlation between the total currents on the antenna and the modal weighting coefficients of the nth mode at ith port, respectively [29].

To decompose the radiation pattern into different modal patterns, the complex correlation coefficient (CCC) between feed patterns $\mathbf{E}^m$ ($m = 1, 2$) and modal patterns $\mathbf{E}_n$ ($n = 1, 2, 3$) can be calculated [30]

$$\rho_{m,n} = \frac{\langle \mathbf{E}^m, \mathbf{E}_n \rangle}{\sqrt{\langle \mathbf{E}^m, \mathbf{E}^m \rangle}\sqrt{\langle \mathbf{E}_n, \mathbf{E}_n \rangle}}, \qquad (12)$$

where $\mathbf{E}^m$ denotes as the electric fields produced by $\mathbf{J}^m$, and $\mathbf{J}^m$ denotes as the surface current on the MIMO antenna when the mth port is excited. From Table I, it is observed that $\rho_{1,1} \simeq \rho_{2,1}$ and $\rho_{1,2} \simeq -\rho_{2,2}$ and Modes 1 and 2 are confirmed as the dominant modes. It is found that the power radiated by these two modes is 99% of the total radiated power, and they contribute equally to each embedded radiation pattern. From the excited current distributions shown in Fig. 3, the Y-shaped patch provides a bilateral symmetric platform for two-port excitations.

(a)   (b)

Fig. 3. Excited current of folded Y-shaped patch antenna at 2.35 GHz. Ports 1 to 2 correspond to subplots (a)-(b).
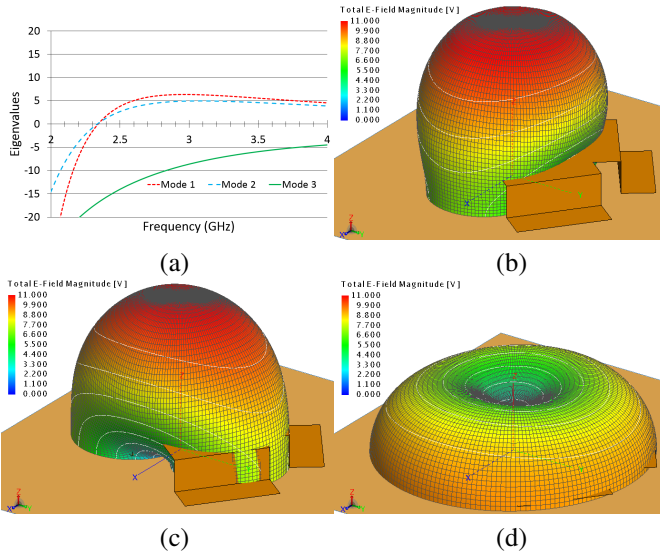

(a)   (b)

(c)   (d)

Fig. 2. (a) Eigenvalues of first three CMs; modal radiation patterns of folded Y-shaped plate at 2.35 GHz. Modes 1 to 3 correspond to subplots (b)-(d).

TABLE I
COMPLEX CORRELATION BETWEEN EMBEDDED RADIATION PATTERNS AND CHARACTERISTIC FAR-FIELD PATTERNS OF Y-SHAPED PATCH.

	Mode 1	Mode 2	Mode 3
Port 1	$0.711\underline{/71.2°}$	$0.701\underline{/67.0°}$	$0.057\underline{/176.3.0°}$
Port 2	$0.710\underline{/71.2°}$	$0.702\underline{/-112.9°}$	$0.057\underline{/176.3°}$

IV. PROPOSED COMPACT THREE-PORT ANTENNA

With the aid of CM analysis, it is shown for the two-port Y-shaped patch that the two dominant modal radiation patterns (which contribute to 99% of the total radiated power) are both pointing in the broadside direction. Therefore, the two radiation patterns excited by the two ports are also
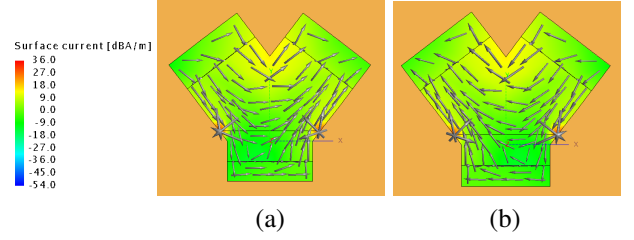
broadside. On the other hand, it can also be observed that the characteristic eigenvalue of the third mode is not very far away from zero in the frequency band of interest. Therefore, it can be expected that the Y-shaped patch has the potential to excite three modes simultaneously if modified appropriately. Another observation is that the third mode of the Y-shaped patch has a monopole-like modal radiation pattern as depicted in Fig. 2(d). Hence, a relatively round-shaped radiator should help to enhance this mode. In the following, the operating mechanism of the two-port antenna is used as a guide for adding an extra port while achieving broadside pattern for all three ports.

A. Structural Modification and Feed Design Using TCM

Although Mode 3 has low modal significance in the Y-shaped patch antenna, it is of interest for the design of a three-port antenna. To enhance Mode 3, it is noted that its characteristic current flows radially outward from the center. Moreover, its electric field is strong and uniform over the top side. These properties resemble those seen on the top plate of a top-loaded monopole antenna, upon excitation. The monopolar operation of this mode is further confirmed by its far-field pattern, shown in Fig. 2(d). Therefore, to enhance Mode 3's monopolar properties, a capacitive loading plate with shorting pins was added just under the top plate. This step successfully brought the Mode 3 resonant frequency down to 3.4 GHz.

To further reduce the resonant frequency of Mode 3 towards that of Modes 1 and 2, its radially outward flowing current pointed to the need for a symmetric structure that supports this current flow. Consequently, the number of branches was increased from three (Y-shaped) to six (snowflake-shaped), and the branches were made rotationally symmetrical (see Fig. 4). This brought the Mode 3 resonant frequency to 2.7 GHz (see Fig. 4(g)), which is close to that for Modes 1 and 2, as seen in Fig. 4(g). Comparing Fig. 2(a) and Fig. 4(g), it is also noted that structural changes to enhance Mode 3 also marginally increase the resonant frequency of Modes 1 and 2 from around 2.3 GHz to 2.85 GHz. However, the modal properties remain the same for these two modes, including orthogonal currents and broadside far-field patterns. Figure 5 shows the far-field patterns of Modes 1 to 3 at 2.85 GHz, which are similar to those of Figs. 2(b)-(d), in which the first two modes exhibit broadside radiation. Other CMs can be ignored as their eigenvalues are much larger in magnitude.

To determine the port location for capacitive feeding, the z-directed characteristic electric field distributions for Modes 1 to 3 were inspected. To excite all three modes simultaneously,
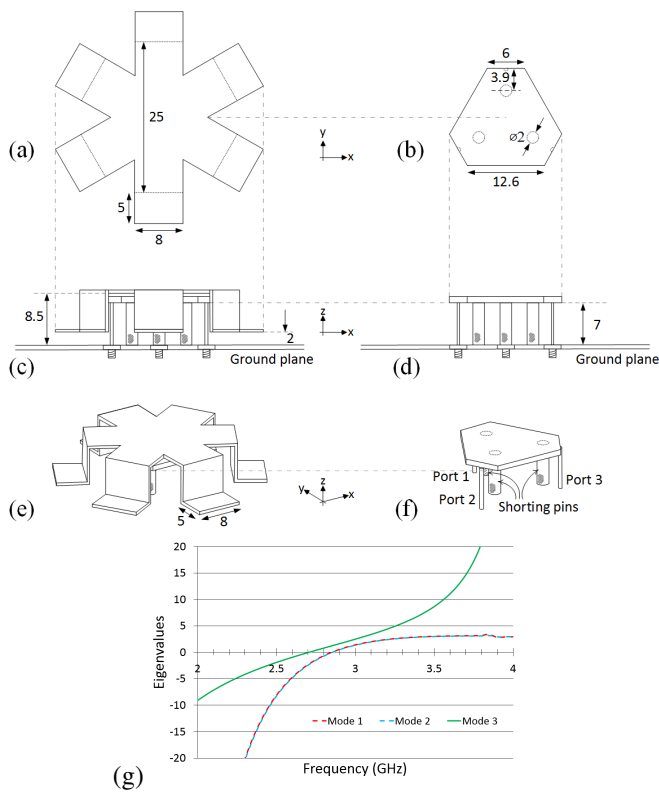
Fig. 4. Proposed compact three-port patch antenna (a) plan view (units: mm); (b) plan view without folded snowflake-shaped radiator; (c) side view; (d) side view without folded snowflake-shaped radiator; (e) perspective view; (f) perspective view without folded snowflake-shaped radiator and (g) eigenvalues of first three CMs.

the z-directed ports should be located where the fields are strong for all three modes. Based on the amplitude of the electric field distribution, suitable locations are along the "branches" close to the folded edges. Adding the constraint of symmetrical port design (as in the Y-shaped case), this means locating a port at every second "branch" of the snowflake-shaped structure, resulting in the candidate locations for each port being in one of the rectangular boxes shown in Fig. 6 (the folded vertical edges are shown as solid black lines in the figure).

The phase distributions of the z-directed characteristic electric fields in Fig. 6 provides further insight on how to generate orthogonal radiation patterns, when all three modes are simultaneously excited. As for the Y-shaped antenna, where (11) shows that phase difference in the excitation of a mode by any two ports contribute to decorrelation, we apply the same principle to the snowflake-shaped structure.

With the amplitude distribution giving the candidate locations for the three ports, Port 1 is first assumed to be located inside the red box in Fig. 6 as a reference point. If Port 2 is located at the green box region, then there is a nearly 180° phase shift between the excitation of Mode 1 by Ports 1 and 2 (resulting in a negative term in the summation of (11)). In contrast, the phase of these two ports (in the red and green boxes) are similar for Modes 2 and 3, contributing to two positive terms. With the port locations being chosen near the edge of the capacitive loading plate, the summation

of the two positive terms are almost equal in magnitude to the negative term, resulting in the orthogonal radiation patterns between Ports 1 and 2. This trend in the excitation of the 3 modes can be confirmed in Table II, which shows the complex correlation coefficients between a port pattern to a modal pattern (i.e., normalized modal weighting coefficient). Due to the symmetrical structure, no further effort is needed to ensure that orthogonal patterns between Ports 1 and 3 as well as Ports 2 and 3 can be achieved by simply copying the same port location in the red or green box to the blue box (for Port 3).

TABLE II
COMPLEX CORRELATION BETWEEN EMBEDDED RADIATION PATTERNS AND CHARACTERISTIC FAR-FIELD PATTERNS OF SNOWFLAKE-SHAPED PATCH.

	Mode 1	Mode 2	Mode 3
Port 1	$0.541\underline{/44.6^\circ}$	$0.587\underline{/-137.4^\circ}$	$0.574\underline{/-143.6^\circ}$
Port 2	$0.784\underline{/-137.2^\circ}$	$0.231\underline{/-140.9^\circ}$	$0.586\underline{/-144.5^\circ}$
Port 3	$0.257\underline{/40.6^\circ}$	$0.780\underline{/41.1^\circ}$	$0.589\underline{/-144.0^\circ}$

In summary, the decorrelation effect between different ports is contributed by the 180° phase shift between the excitation of Modes 1 and 2 by the different ports, with the 180° phase difference resulting in the reduction of the correlation as predicted by (11). In contrast, the electric field of Mode 3 offers the same phase for excitation at all three port regions.

B. Antenna Structure

Based on the design procedure in Section IV-A, the Y-shaped patch antenna [10] was evolved into a snowflake-shaped patch radiator (see Fig. 4). Like the Y-shaped antenna, it also has folded structures producing six capacitive loads for miniaturization. The height of the air gap in each capacitive load is 2 mm. The ground plane is made on a circular FR4 epoxy board with diameter 100 mm and having three SubMiniature version A (SMA) connectors soldered on the antenna interface. It is noted that copper can also be used to build the radiator. However, due to the physical constraints and mechanical considerations, aluminum was considered more practical for the construction of the snowflake-shaped patch with folded branches. In addition to the capacitive loads, capacitive feeds are opportunistically introduced using the capacitive loading plate under the main patch to achieve better impedance matchings. The capacitive loading plate is a hexagonal copper patch, as depicted in Fig. 4(b). The material thicknesses of the snowflake-shaped and the hexagonal patches used are 0.5 mm and 1.0 mm, respectively. Furthermore, three 7 mm-long copper shorting pins with diameters of 2 mm are evenly distributed next to the three feeding probes, as shown in Figs. 4(b) and (d). A perspective view of the inner structure can also be seen in Fig. 4(f), which shows three antenna probes connected to the hexagonal patch, but not touching anything else. The snowflake-shaped patch is suspended in the air at the top, such that it is excited by the capacitive coupling of the non-contact hexagonal patch underneath. If the proposed three-port antenna is made with a regular hexagonal ground plane, the entire antenna structure is not only rotationally symmetric by 120 degrees, but also scalable to any number of antennas in the xy-plane.
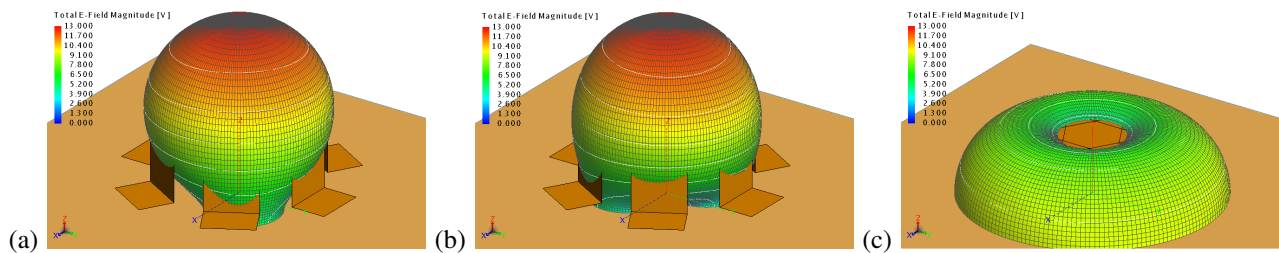
Fig. 5. Modal radiation patterns of the folded snowflake-shaped plate at 2.85 GHz. Modes 1 to 3 correspond to subplots (a)-(c).
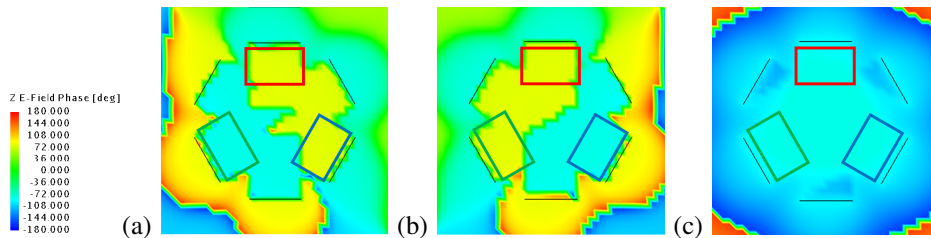

Fig. 6. Phase distribution of z-directed characteristic electric fields 1 mm under the top part of the folded snowflake-shaped plate at 2.85 GHz. Modes 1 to 3 correspond to (a)-(c).

C. Antenna Performance

Our three-port design concept was validated by full-wave simulation and experiment. The simulations are all based on the time-domain solver of CST [27]. Experimental results were obtained from a prototype of the design.

The simulation results reveal that the antenna resonates at 2.88 GHz, as depicted in Fig. 7(a), which agrees well with the calculated modal resonances. The 10 dB impedance bandwidth is 5.2% and the coupling coefficient between any two ports is lower than -16 dB within this band. Figures. 8(a)-(c) show three 2-D cuts of simulated radiation patterns in xz-, yz- and xy-planes for Port 1. A broadside radiation pattern pointing in the $+z$ direction is obtained. The pattern null at 240° in the yz-plane is due to the presence of shorting pins. As Ports 2 and 3 of the snowflake-shaped patch antenna do not lie on the xz- nor yz-planes, so the 2D pattern cuts look different to those of Port 1. However, with 120° rotations of the antenna around the z-axis, the 2D-pattern cuts of Ports 2 and 3 will then be identical to that of Port 1.

Figure 7(b) reveals that the resonant frequency is shifted marginally (i.e., by 5.9%) to 3.05 GHz relative to the simulated resonance at 2.88 GHz. The discrepancy can be attributed to fabrication tolerances including soldering, tolerance of folded structure in the snowflake-shaped radiator, and tolerance of air gap size between the snowflake-shaped patch radiator and the hexagonal feeding patch. To investigate the fabrication tolerances, some additional simulations were performed. From these simulation result, it was found that soldering metals can increase the antenna resonant frequency by 1% to 2.91 GHz. In addition, it was difficult to fold the snowflake branches by hand, and it also resulted in a small reduction in metal length at each fold. According to the simulation, if the length is reduced by 0.2 mm at each fold (i.e., 0.8 mm in total across each branch), this factor alone will increase the simulated resonance by 3% (to 2.96 GHz). Indeed, the reduction in the length of the actual prototype was measured to be 0.9 mm.

Furthermore, if only the air gap size between the snowflake-shaped patch radiator and the hexagonal feeding patch was increased by 0.2 mm, this change will increase the simulated resonant frequency by 2.5% (to 2.95 GHz). Therefore, the frequency shift can be fully accounted for by these three error sources. The manufacturing accuracy can be improved by 3D metal printing or prototyping in a commercial workshop.

Nevertheless, very similar frequency responses were obtained and the coupling coefficient of less than -17 dB was maintained experimentally. From the measurement results, the 10 dB impedance bandwidth of 4.3% is achieved, which is slightly smaller than the simulated bandwidth of 5.2%. Relative to the wavelength in air, the largest lateral dimension and height of the antenna are $0.36\lambda_o$ and $0.09\lambda_o$, respectively.

The proposed antenna is smaller in patch surface area than a conventional patch antenna mainly because of the folded structure and the capacitive loading effect. One key contribution of this novel antenna design is that a compact single metal structure can generate three broadside radiation patterns simultaneously. This pattern shape was confirmed experimentally using a Satimo StarLab system. Three sets of radiation patterns were measured at 3.05 GHz and 2-D cuts of realized gains in xz-, yz- and xy-planes were obtained and are provided in Figs. 8(d)-(f) for Port 1. It should be noted that when a given port was under test, the other two ports were terminated with 50Ω loads. Broadside and rather symmetric radiation patterns are observed in xz- and yz-planes, which agree well with the simulated results. The pattern null at 240° in the yz-plane is also present in the measurement. The excited current distributions for Ports 1 to 3 are also provided in Fig. 9 for reference.

The antenna efficiency and gain of Ports 1 to 3 are provided in Fig. 7(c). The measured peak efficiency and gain at 3.05 GHz are 96.0% and 6.9 dBi, respectively. The envelope correlation (magnitude of CCC squared) of any two antenna ports was calculated with simulated radiation patterns and the

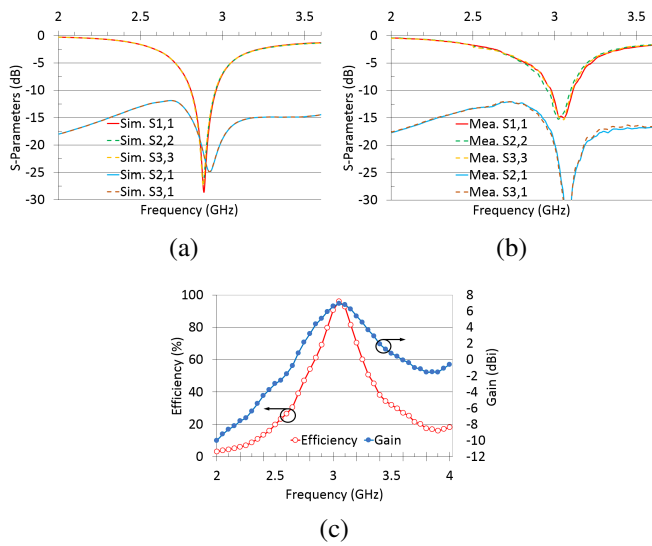envelope correlation is below 0.1 in the frequency band of interest.

Fig. 7. (a) Simulated S-parameters; (b) measured S-parameters and (c) measured efficiency and gain of proposed compact three-port patch antenna.

D. Further Validation and Diversity Mechanism of Proposed Design

The three-port snowflake-shaped antenna designed with the TCM based procedure was analyzed to verify that the available modes are correctly utilized to achieve the desired properties of orthogonal patterns and broadside radiation. The CCCs between $\mathbf{E}^m$ ($m = 1, 2, 3$) and $\mathbf{E}_n$ ($n = 1, 2, 3$) were computed to decompose the radiation pattern into different CMs (see Table II). From Table II, it is noticed that $\rho_{1,3} \simeq \rho_{2,3} \simeq \rho_{3,3}$, which implies the embedded radiation pattern of each port has the same contribution from the third modal pattern (roughly 1/3 of the total power), subject to small numerical errors.

The relative power radiated by each mode for a given port is given by the magnitude square of the complex correlation value. The results show that the power radiated by the first two modes combined and the third mode are 66% and 34% of the total radiated power, respectively, for any given port. The first two dominant CMs offer broadside radiation and the third mode is used to facilitate orthogonality between ports leading to low mutual coupling and correlation among the ports.

Furthermore, antenna diversity can be generally categorized as pattern (or angle), spatial and polarization diversity [31]. In our proposed snowflake-shaped patch antenna, the patterns excited by three ports are all broadside radiation and relatively low pattern diversity is expected. To isolate the respective contributions from spatial and polarization diversity of our proposed antenna, spatial diversity can be removed from the complex radiation patterns with the following procedure. First, the phase center of each port is calculated (available as a standard feature in CST [27]). Then, selecting the phase center of one port as the reference position we can extract the radiation pattern of this port at 2.88 GHz. Then, move the physical antenna model along x- and y- directions (without

any rotation) so that the phase center of another port aligns with the reference position. The radiation pattern of this second port is then extracted by simulation. Finally, repeat this step for the third port. Then, the calculated magnitude of CCC between any two of these three radiation patterns is found to be 0.28 (0.01 if no phase center shift to a common point), which indicate that space diversity plays a significant role in further reducing antenna correlation. Furthermore, from the modal current distributions shown in Fig. 10, it is observed that the currents of Modes 1 and 2 are dominantly flowing from top right corner to bottom left corner and from bottom right corner to top left corner, respectively. On the other hand, the currents at Mode 3 are flowing radially outward. It should be emphasized that the first three CMs have all contributed to the orthogonal radiation patterns of the proposed three-port antenna. Mode 3, despite its non-broadside pattern as illustrated in Fig. 5(c), enables the three antenna ports with broadside radiation to be achieved with low pattern correlation. To conclude, we show the potential of employing a third mode to achieve low correlation for a three-port antenna while maintaining the desired broadside radiation.

V. MASSIVE MIMO ANTENNA

The proposed compact three-port antenna is a regular snowflake shape, therefore it can be tessellated to form a massive MIMO antenna. When compared to a massive MIMO antenna consisting of conventional two-port dual-polarized patch radiators, the main advantage of the proposed design is that a third port, also with broadside radiation, is available. As first demonstration for massive MIMO application, a 21-port antenna (group of seven three-port antennas) is investigated and the target maximum inter-element coupling coefficient is set around -15 dB. This prototype allows key array parameters to be evaluated, especially the effects of interactions among unit cells. Simulation results for a 102-port antenna (group of 34 three-port antennas) are also provided to demonstrate their effectiveness in a massive MIMO context.

A. 21-Port Array Simulation and Experiment

To allow the proposed three-port antenna to become a basic unit cell for building a massive MIMO antenna, the shape of the ground plane was changed to a regular hexagon. Then, seven of the three-port antennas were tessellated, as illustrated in Fig. 11. The associated antenna port numbers are also given in Fig. 11(a), where all snowflake-shaped radiators are hidden for better illustration. Theoretically, the idea can be extended to any number of unit cells (34-cell version explored in Section-V.B). All dimensions and materials used in the individual antenna construction are the same as those described in Section IV.

Figure 12 provides the results for the measured S-parameters. Due to symmetry, only the reflection coefficient and coupling coefficients relating to Port 1 are provided. It can be seen that the antennas operate at 3.00 GHz with low intra- and inter-element mutual couplings. Simulations obtained using CST [27] provide an estimated resonant frequency of 2.88 GHz. The frequency shift between the simulation
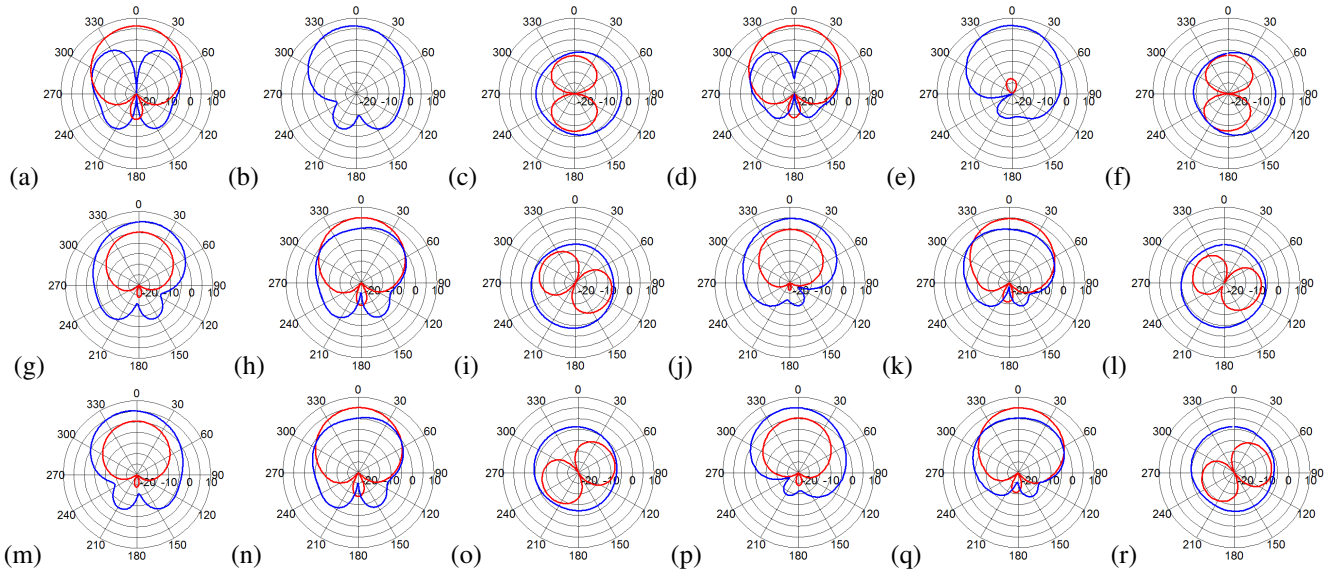
Fig. 8. Radiation patterns of proposed compact three-port patch antenna obtained at 2.85 GHz with E-phi (red) and E-theta (blue). Port 1: (a)-(f); Port 2: (g)-(l) and Port 3: (m)-(r). xz-plane: (a), (d), (g), (j), (m) and (p); yz-plane (b), (e), (h), (k), (n) and (q); xy-plane (c), (f), (i), (l), (o) and (r). Simulation: (a)-(c), (g)-(i) and (m)-(o); Measurement: (d)-(f), (j)-(l) and (p)-(r).
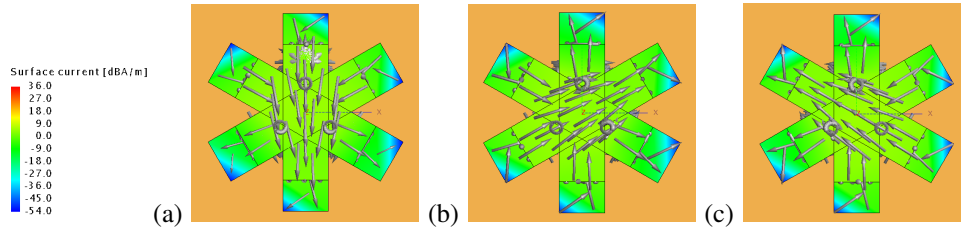

Fig. 9. Excited current of proposed snowflake-shaped patch antenna at 2.85 GHz. Ports 1 to 3 correspond to (a)-(c).
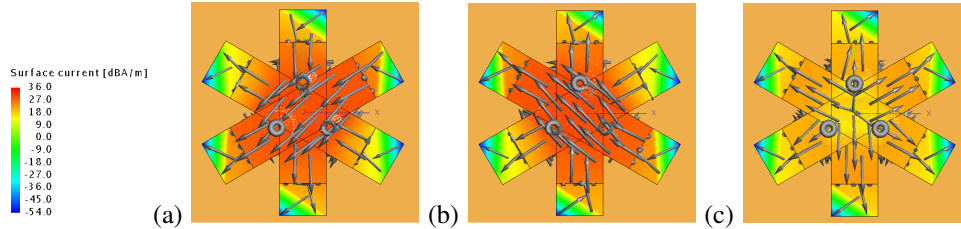

Fig. 10. Modal current of the folded snowflake-shaped plate at 2.85 GHz. Modes 1 to 3 correspond to subplots (a)-(c).

and experiment is mainly due to soldering and fabrication tolerances. The inter-element edge-to-edge separation is 25 mm, equivalent to $0.25\lambda_o$ at 3.00 GHz. The inter-element center-to-center separation is 60 mm, which corresponds to $0.6\lambda_o$. This is close to conventional antenna array elements having about half wavelength unit-cell separation. However it should be emphasized that each unit cell in the proposed design consists of three antenna ports rather than just two ports as in dual-polarized designs. Moreover, half-wavelength separation is not a requirement for massive MIMO operation. In fact, larger separation increases diversity gain in general.

Within the 10 dB impedance bandwidth, the intra-element mutual coupling is lower than -17 dB, whereas the inter-element mutual couplings are all below -14 dB. More importantly, most coupling coefficients are smaller than -20 dB and some achieve -25 dB depending on separation distances

and relative positionings of the ports. Similar to the case of a single three-port antenna, relatively broadside and symmetrical radiation patterns are observed in the xz- and yz-planes in the array configuration. The considerable distortion found in the xy-plane comes from interactions with the nearby radiating elements. The corresponding measured antenna efficiency and gain curves are also similar to the single element configuration but the maximum efficiency is reduced to approximately 70% and the maximum gain to 4 dBi. The degradation of antenna efficiency and gain at Port 1 (as compared to the single-antenna case) are mainly due to the coupling loss via Ports 5, 6, 8 and 21. The building of half-wavelength choke walls on the ground plane may help to further improve isolation between neighboring elements [8]. However, in this first demonstration study, the main purpose is to demonstrate the main characteristics of the proposed antenna in a massive MIMO configuration, hence

a plain ground plane without any mutual coupling reduction techniques is considered sufficient.
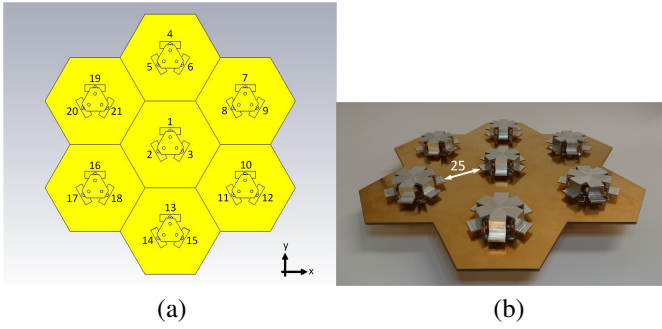

Fig. 11. Geometry of seven three-port snowflake-shaped patch antennas in an array arrangement: (a) port arrangement; (b) prototype (units: mm).
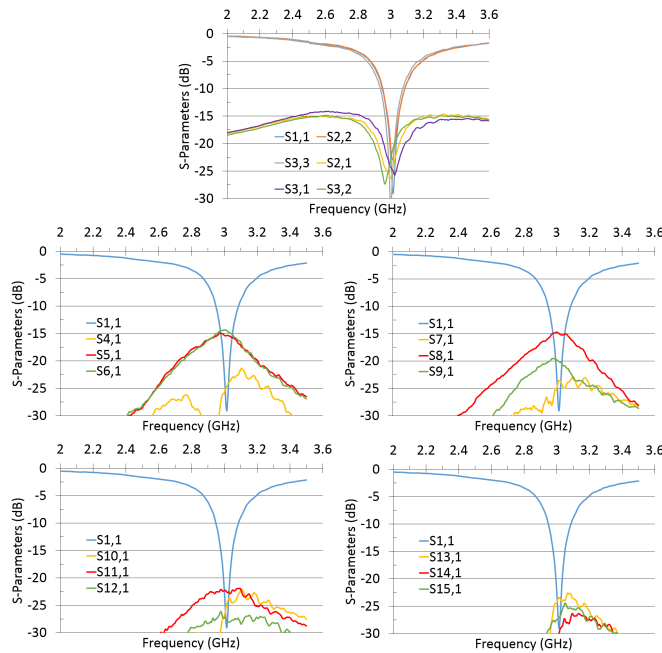

Fig. 12. Measured S-parameters of seven integrated three-port snowflake-shaped patch antennas.

B. 102-Port Array System Simulation

To form a realistic massive MIMO array, 34 of the three-port element were tessellated into a 102-port massive MIMO array in full-wave simulations. The system level performance of the proposed MIMO array was evaluated in a multi-user MIMO (MU-MIMO) system by combining the simulated array antenna properties with a standard channel model in Matlab.

The base station was assumed to have $M = 102$ antennas, simultaneously serving $K = 5$ users and each user only has one antenna. The performance of the MU-MIMO reverse link is considered so that the propagation matrix is a $M \times K$ matrix denoted as $\mathbf{H}$. Assuming a Kroneckor channel model [32]

$$\mathbf{H} = \mathbf{R}^{1/2}\mathbf{H}_\mathrm{w} \qquad (13)$$

where $\mathbf{H}_\mathrm{w}$ is a $M \times K$ matrix containing independent and identically distributed (IID) zero mean complex Gaussian random variable with unity variance and $\mathbf{R}$ denotes the correlation matrix of the M antennas in the base station. This approach fully captures the effects of the antennas on the channel [32] so that we can write

$$\mathbf{R} = \mathbf{\Lambda}^{1/2}\bar{\mathbf{R}}\mathbf{\Lambda}^{1/2} \qquad (14)$$

where $\bar{\mathbf{R}}$ is a normalized correlation matrix whose diagonal elements are unity, and the (i, j)th ($i \neq j$) element denotes the complex correlation coefficient between the 3-D radiation patterns of the ith and jth antenna ports. $\mathbf{\Lambda}$ denotes a diagonal matrix given by $\mathbf{\Lambda} = \mathrm{diag}\left[\eta_1, \eta_2, \ldots, \eta_M\right]$ where η_i is the total efficiency of the ith antenna port. Therefore $\mathbf{R}$ fully characterizes the efficiency, efficiency imbalance, and correlation among the receive antennas [32].

For massive MIMO arrays, an important property is the quantity [1]

$$\frac{\mathbf{H}^H\mathbf{H}}{M}, \qquad (15)$$

which tends to $\mathbf{I}_K$ ($\mathbf{I}_K$ denotes the $K \times K$ identity matrix) with increasing M and it represents one major benefit of massive MIMO (useful for receiver decoding). To evaluate (15), multiple random realizations of $\mathbf{H}$ are generated and an error based metric, $\Delta = \left\|\frac{\mathbf{H}\mathbf{H}^H}{M} - \mathbf{I}_K\right\|_F / K$, is computed for each realization where $\|\ \|_F$ is the Frobenius norm. The error metric quantifies the departure of the channel property from the desired property. The simulation results for our 102-port and 21-port arrays are shown in Fig. 13. Comparisons with ideal 102- and 21-port arrays are also provided (ideal antenna arrays are assumed to be 100% efficient and $\mathbf{R}$ is taken as the identity matrix). It can be seen that when the number of antennas in the base station is large, $\frac{\mathbf{H}^H\mathbf{H}}{M}$ is approximately $\mathbf{I}_K$, demonstrating good massive MIMO performance. For example, for the 102-port antenna, the error-based metric Δ is approximately 0.1, but for the smaller 21-port antenna, Δ is greater than 0.2. Moreover, these values are very close to those of the ideal antennas obtained when $\mathbf{H} = \mathbf{H}_\mathrm{w}$.

The sum rate of the reverse link was also simulated for the multiuser massive MIMO system. The same signal-to-noise ratio (SNR), denoted as ρ, is assumed for each user and the following sum rate expression is utilized [1]

$$C_\mathrm{sum} = \log_2 \det\left(\mathbf{I}_K + \rho\mathbf{H}^H\mathbf{H}\right). \qquad (16)$$

In the simulation, the same 21- and 102-port scenarios were again compared. The Monte Carlo method was used to generate 10,000 channel realizations and the ergodic sum rate were computed and shown in Fig. 13. As can be seen, the ergodic sum rate achieved by using the proposed massive MIMO array is close to the ergodic sum rate achieved by using ideal antenna arrays (i.e., ~1-2 dB gap at a given sum rate). In addition, as can be expected, using more antenna at the base station leads to a higher ergodic sum rate.
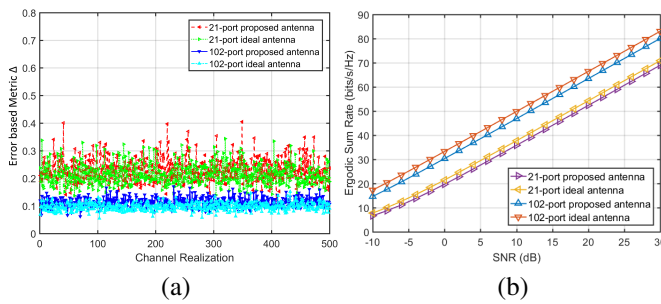
Fig. 13. Simulation results of (a) Frobenius norm of error relative to perfectly orthogonal massive MIMO channel and (b) Ergodic sum rate of the reverse link massive MIMO system.

VI. CONCLUSION

In this article, TCM is used to analyze an existing two-port Y-shaped antenna. The insights obtained were then utilized to extend the design to an efficient compact three-port MIMO antenna with broadside patterns and low correlation. By tessellating together the three-port element to form 21- and 102-port arrays, key characteristics that make the design suitable for massive MIMO applications were also demonstrated.

The existing two-port Y-shaped patch antenna was modified into a snowflake-shaped patch antenna and excited by three ports via capacitive coupling. The first two modal patterns with broadside radiation were equally shared by three ports. Mode 3, despite its non-broadside pattern, enables the three antenna ports with broadside radiation to be achieved with low pattern correlation. Without employing any coupling suppression technique, defected ground structures, choke walls or decoupling networks, the experimental results show that the intra- and inter-element coupling coefficients are lower than –17 dB and -14 dB, respectively for a 21-port prototype. The maximum lateral dimension of the canonical three-port element is $0.36\lambda_o$, which results from antenna miniaturization using six capacitive loads in the structure. It is also shown by simulation that a 102-port massive MIMO array based on this 3-port element achieves similar channel orthogonality as the reference case of an ideal IID multiuser channel of a similar size.

REFERENCES

[1] F. Rusek, D. Persson, B. K. Lau, E. G. Larsson, T. L. Marzetta, O. Edfors, and F. Tufvesson, "Scaling up MIMO: Opportunities and challenges with very large arrays," *IEEE Signal Process. Mag.*, vol. 30, no. 1, pp. 40–60, Jan., 2013.

[2] E. G. Larsson, O. Edfors, F. Tufvesson, and T. L. Marzetta, "Massive MIMO for next generation wireless systems," *IEEE Commun. Mag.*, vol. 52, no. 2, pp. 186–195, 2014.

[3] L. Lu, G. Y. Li, A. L. Swindlehurst, A. Ashikhmin, and R. Zhang, "An overview of massive MIMO: Benefits and challenges," *IEEE J. Sel. Topics in Signal Process.*, vol. 8, no. 5, pp. 742–758, Aug., 2014.

[4] L. U. Choi and R. D. Murch, "A transmit preprocessing technique for multiuser MIMO systems using a decomposition approach," *IEEE, Trans. Wireless Com.*, vol. 3, no. 1, pp. 20–24, Jan., 2004.

[5] C. Y. Chiu, J. B. Yan, R. D. Murch, J. X. Yun, and R. G. Vaughan, "Design and implementation of a compact 6-port antenna," *IEEE Antennas Wireless Propag. Lett.*, vol. 8, pp. 767–770, 2009.

[6] S. Chen and K. M. Luk, "A dual-mode wideband MIMO cube antenna with magneto-electric dipoles," *IEEE Trans. Antennas Propag.*, vol. 62, no. 12, pp. 5951–5959, Dec., 2014.

[7] A. MoradiKordalivand, T. A. Rahman, and M. Khalily, "Common elements wideband MIMO antenna system for WiFi/LTE access-point applications," *IEEE Antennas Wireless Propag. Lett.*, vol. 13, pp. 1601–1604, 2014.

[8] D. Manteuffel and R. Martens, "Compact multimode multielement antenna for indoor UWB massive MIMO," *IEEE Trans. Antennas Propag.*, vol. 64, no. 7, pp. 2689–2697, Jul., 2016.

[9] S. Stein, "On cross coupling in multiple-beam antennas," *IRE Trans. Antennas Propag.*, vol. 10, no. 5, pp. 548–557, Sep., 1962.

[10] S. C. Ko and R. D. Murch, "Compact integrated diversity antenna for wireless communications," *IEEE Trans. Antennas Propag.*, vol. 49, no. 6, pp. 954–960, Jun., 2001.

[11] T. W. Chiou and K. L. Wong, "Broad-band dual-polarized single microstrip patch antenna with high isolation and low cross polarization," *IEEE Trans. Antennas Propag.*, vol. 50, no. 3, pp. 399–401, Mar., 2002.

[12] Z. N. Chen and Y. W. Chia, "Experimental study on radiation performance of probe-fed suspended plate antennas," *IEEE Trans. Antennas Propag.*, vol. 51, no. 8, pp. 1964–1971, Aug., 2003.

[13] C. Y. D. Sim, C. C. Chang, and J. S. Row, "Dual-feed dual-polarized patch antenna with low cross polarization and high isolation," *IEEE Trans. Antennas Propag.*, vol. 57, no. 10, pp. 3405–3409, Oct., 2009.

[14] D. Pinchera and F. Schettino, "A dual-polarized parasitic patch antenna for MIMO systems," in *Proc. 39th Europ. Microw. Conf. (EuMC)*, Rome, Italy, Sep. 29-Oct. 1, 2009, pp. 642–644.

[15] Y. Gao, R. Ma, Y. Wang, Q. Zhang, and C. Parini, "Stacked patch antenna with dual-polarization and low mutual coupling for massive MIMO," *IEEE Trans. Antennas Propag.*, vol. 64, no. 10, pp. 4544–4549, Oct., 2016.

[16] G. L. Wu, W. Mu, G. Zhao, and Y. C. Jiao, "A novel design of dual circularly polarized antenna fed by L-strip," *Progress Electromag. Research (PIER)*, vol. 79, pp. 39–46, 2008.

[17] Z. Harouni, L. Cirio, L. Osman, A. Gharsallah, and O. Picon, "A dual circularly polarized 2.45-GHz rectenna for wireless power transmission," *IEEE Antennas Wireless Propag. Lett.*, vol. 10, pp. 306–309, 2011.

[18] J. H. Chou, D. B. Lin, K. L. Weng, and H. J. Li, "Novel T-shape slot couple feed dual circular polarized rectenna," in *Proc. Int. Symp. Antennas Propag. (ISAP'2012)*, Nagoya, Japan, Oct. 29- Nov. 2, 2012, pp. 178–181.

[19] Z. Miers, H. Li, and B. K. Lau, "Design of bandwidth-enhanced and multiband MIMO antennas using characteristic modes," *IEEE Antennas Wireless Propag. Lett.*, vol. 12, pp. 1696–1699, 2013.

[20] ——, "Design of bezel antennas for multiband MIMO terminals using characteristic modes," in *Proc. 8th Europ. Conf. Antennas Propag. (EuCAP'2014)*, Hague, Netherlands, Apr. 6-10, 2014, pp. 2556–2560.

[21] R. Garbacz, "Modal expansions for resonance scattering phenomena," *Proc. IEEE*, vol. 53, no. 8, pp. 856–864, 1965.

[22] R. Garbacz and R. Turpin, "A generalized expansion for radiated and scattered fields," *IEEE Trans. on Antennas Propag.*, vol. 19, no. 3, pp. 348–358, May, 1971.

[23] R. Harrington and J. Mautz, "Theory of characteristic modes for conducting bodies," *IEEE Trans. Antennas Propag.*, vol. 19, no. 5, pp. 622–628, Sep., 1971.

[24] ——, "Computation of characteristic modes for conducting bodies," *IEEE Trans. Antennas Propag.*, vol. 19, no. 5, pp. 629–639, Sep., 1971.

[25] H. Li, Z. T. Miers, and B. K. Lau, "Design of orthogonal MIMO handset antennas based on characteristic mode manipulation at frequency bands below 1 GHz," *IEEE Trans. Antennas Propag.*, vol. 62, no. 5, pp. 2756–2766, May., 2014.

[26] K. K. Kishor and S. V. Hum, "A two-port chassis-mode MIMO antenna," *IEEE Antennas Wireless Propag. Lett.*, vol. 12, pp. 690–693, 2013.

[27] CST Microwave Studio, CST Studio Suite TM, 2017.

[28] FEKO 14.0, Altair Engineering Inc., 2016.

[29] K. K. Kishor, "Multi-functional chassis-based antennas using characteristic mode," PhD thesis, Department of Electrical and Computer Engineering, University of Toronto, 2014, ch. 2.

[30] E. Safin and D. Manteuffel, "Reconstruction of the characteristic modes on an antenna based on the radiated far field," *IEEE Trans. Antennas Propag.*, vol. 61, no. 6, pp. 2964–2971, Jun., 2013.

[31] R. Tian, V. Plicanic, B. K. Lau, and Z. Ying, "A compact six-port dielectric resonator antenna array: MIMO channel measurements and performance analysis," *IEEE Trans. Antennas Propag.*, vol. 58, no. 4, pp. 1369–1379, Apr., 2010.

[32] R. Tian, B. K. Lau, and Z. Ying, "Multiplexing efficiency of MIMO antennas," *IEEE Antennas Wireless Propag. Lett.*, vol. 10, pp. 183–186, 2011.